ORIGINAL PAPER

CrossMark

Structural and Soft Magnetic Properties of Nickel-Substituted Co-Zn Nanoferrites

B. B. V. S. Vara Prasad[1] · K. V. Ramesh[2] · Adiraj Srinivas[3]

Abstract

Nickel-substituted cobalt-zinc nanoferrites ($Co_{0.5-x}Zn_{0.5}Ni_xFe_2O_4$, $x = 0.05$ to 0.25 in steps of 0.05) were synthesized in a citric acid auto-combustion method. Divalent strong paramagnetic nickel ions substituted in place of ferromagnetic cobalt ions resulted in slight modifications over structural and significant changes in magnetic properties of the system. All samples were characterized with X-ray diffraction technique for structure determination. Crystallite sizes were calculated using the Williamson-Hall plot and size-strain plots, from these lattice strain and microstrain were discussed. Transmission electron microscopy measurements were done for the base sample ($x = 0$), and they showed well-developed spherical particles with an average size of 35 nm. SEM micrograph was recorded for the base sample to observe surface morphology, and it was observed to be stoichiometric, as evident from EDAX measurements. Saturation magnetization, remanence, coercivity and remanence ratio were measured using M-H loops recorded using a vibrating sample magnetometer at room temperature. Magnetocrystalline anisotropy was discussed with the help of magnetocrystalline anisotropy constant (K_1) obtained from the law of approach to saturation method.

1 Introduction

In the history of material science and engineering, the study of nanomaterials opened a path way for new applications. Nano became a synonym for nirvana in the perspective of technological applications. The importance of nanomaterials lies in the structural properties as the size plays a vital role in determining their properties and performance. Consequently, miniaturization of devices was made possible by harvesting the key aspects/feature of nanomaterials. As a sub-category, nanomagnetic materials reached another milestone as they achieved remarkable magnetic characteristics. Among nanomagnetic materials, nanoferrites were thoroughly studied with different combinations of cations in several synthesizing routes [1–5]. Cations in a ferrite system are bonded via tetrahedral and octahedral coordination with a closed packed structure of oxygen atoms. The addition/substitution/replacement of cations in the system will drastically change structural ambience, leading to remarkable changes in the bonds and interactions.

Significant contributions were made on nanoferrites to improve their electric and magnetic properties. In the middle of all nanoferrite systems, Ni-Zn nanoferrites are exploited for their usefulness at high frequencies as well as Mn-Zn nanoferrites. Recently, apart from ferrofluid applications such as magnetic hypothermia, cobalt nanoferrites are in the focused area with suitable substitutions to control their high coercivity, remanence and magnetic losses. Among several substitutions, zinc provided a control over the above-said drawbacks with cobalt nanoferrites which made them suitable for power and data storage applications. High permeability, magnetization, low energy losses, low Curie temperature and high anisotropy are the requirements for power and data storage applications [6].

✉ K. V. Ramesh
kvramesh11@gmail.com

1 Department of Physics, MVGR College of Engineering, Vizianagaram, Andhra Pradesh, 535005 India

2 Department of Electronics and Physics, GITAM Institute of Science, Gandhi Institute of Technology and Management (GITAM-Deemed to be University), Visakhapatnam, Andhra Pradesh, 530045 India

3 Defence Metallurgical Research Laboratory, DRDO, Hyderabad, Telangana, 500060 India

The author(s) previously reported [7] the synthesis of base compound ($Co_{0.5}Zn_{0.5}Fe_2O_4$) in auto-combustion route with different chelating agents and discussed the structural and magnetic properties in as-prepared form without any thermal treatment, whereas in this study, the annealed version of the base compound with nickel substitution in place of cobalt is presented and explained in the light of existing understanding. The present series of nickel-substituted Co-Zn nanoferrites was investigated for the changes in structural and magnetic properties. There is only one Bohr magnetons of the spin magnetic moment difference between these two ions, and they have a narrow difference between their cationic radii. Moreover, both have strong octahedral site preference and the simultaneous presence of both ions in the same system leads to interesting structural and magnetic properties.

2 Experimental Details

2.1 Synthesis

Citric acid auto-combustion method was used to synthesize the present series of samples: $Co_{0.5-x}Zn_{0.5}Ni_xFe_2O_4$. Stoichiometric proportions of high-purity raw materials, cobalt nitrate ($Co(NO_3)_2 \cdot 6H_2O$ (99%)), zinc nitrate ($Zn(NO_3)_2 \cdot 6H_2O$ (99.5%)), iron nitrate ($Fe(NO_3)_3 \cdot 6H_2O$ (99.5%)) and citric acid ($C_6H_8O_7 \cdot H_2O$), were weighed and dissolved each material separately in a minimum amount of de-ionized water. Further, as formed metal hydroxide solutions were thoroughly mixed as well as stirred for an hour to improve homogeneity. Citric acid was taken in 1:1 ratio with the metal nitrates, dissolved separately in de-ionized water and added to the metal precursor solution dropwise. This mixture was continuously stirred about an hour until clear brownish solution was obtained. This solution was initially heated about 65 °C under continuous and constant stirring rate. Slowly, the temperature was increased beyond 100 °C and it was kept constant at 135 °C. At the beginning, water was slowly evaporated and, as the time proceeds, viscous liquid was formed, leading to the gelation. Subsequent to gelation, the continuous and constant heat from the hot plate leads to the rise of the internal temperature of the gel and proceeded with the burning of the gel, resulting in the formation of chunks of fluffy product by the releasing of brownish gases. After the completion of the reaction, these flakes were grounded for 1 h (both wet and dry) to achieve fine powder using an agate mortar and pestle. The final powders were annealed at 1000 °C for 4 h at a heating rate of 10 °C per min, followed by natural cooling to room temperature. Prior to measurements, these annealed samples were again grounded for 30 min to obtain fine powders.

2.2 Characterization Techniques

PerkinElmer model Diamond TGA/differential thermal analysis (DTA) instrument was used to record DTA curves of the present samples in the temperature range of 15 to 900 °C with an accuracy of less than ±0.5 °C. Prior to further analysis, the structure and phase were identified using powder X-ray diffraction patterns, which were recorded using a Bruker D8 Advance powder X-ray diffractometer with Cu Kα (λ = 1.5406 Å) radiation to ensure the process adopted was an acceptable one. Particle size measurements were carried out using a transmission electron microscopy (TEM; model FEI Tecnai G2) with an accelerating voltage of 200 kV. Morphological images (SEM micrographs) and energy-dispersive X-ray spectroscopy (EDX) spectra were recorded using a scanning electron microscope (SUPRA 40, Zeiss). Infrared measurements were recorded using a PerkinElmer FTIR spectrometer, and it has a resolution of 1 cm^{-1} and a scan range of 700 to 50 cm^{-1} at room temperature using a KBr pellet. Room-temperature M-H curves were recorded using a LakeShore 7400 vibrating sample magnetometer up to 15,000 Oe. Saturation magnetization, coercivity, remanent magnetization and squareness ratio were acquired from the recorded M-H curve data. For simplicity, the present series of samples are named as B (base, $x = 0$), Ni1 ($x = 0.05$), Ni2 ($x = 0.1$), Ni3 ($x = 0.15$), Ni4 ($x = 0.2$) and Ni5 ($x = 0.25$).

2.3 DTA Analysis

In general, the annealing temperature of nanoferrites has to be above the ferrite crystallization temperature (often referred as ferritization temperature). To find out the range of ferritization temperature, DTA study was performed, which measures changes in temperature between a sample and a reference as it gives the exothermic or endothermic nature of the reaction as a function of temperature or time. The annealing temperature for the current series of samples was determined after conducting DTA analysis, where the crystallization temperature was determined. At around 300 °C, there was a sharp decrease in heat flow indicating the decomposition of nitrates. It is evident from Fig. 1, all samples (B, Ni1, Ni3, Ni5) displayed nearly identical variations in the DTA curves up to 400 °C, after that the residual chelating complex with metal and hydroxide ions eventually burnout and crystallized into final product. All of the samples displayed different crystallization temperatures. The crystallization temperature of the base compound is at 495 °C, while Ni1, Ni3 and Ni5 displayed more than this temperature and below 525 °C, which is well below the crystallization temperature (550 °C) of the same composition [8], and it is attributed to the introduction of nickel as well as the amount of heat energy given to
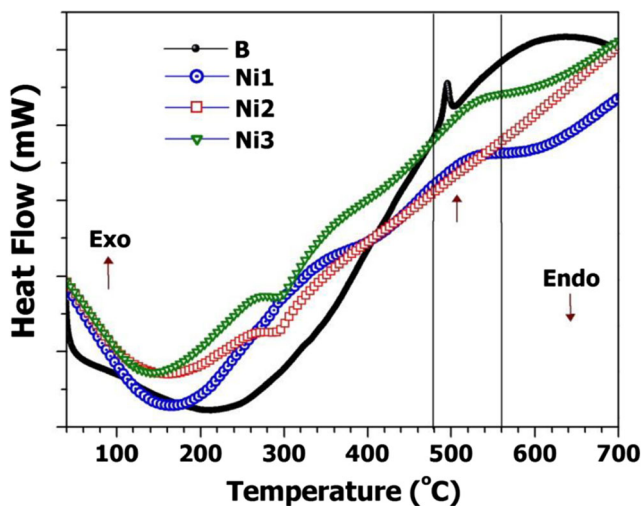
Fig. 1 DTA curves of base, Ni1 ($x = 0.05$), Ni3 ($x = 0.15$) and Ni5 ($x = 0.25$)

Fig. 2 Powder X-ray diffraction patterns of $Co_{1-x}Ni_xZn_{0.5}Fe_2O_4$

the system. The incorporating nickel into the spinel lattice modified the ferritization temperature from 495 °C. To make sure that the well development of grains/particles, the annealing temperature was fixed at a relatively high temperature (1000 °C) for the duration of 4 h, so that for the last sample with a nickel content of $x = 0.25$, the crystallization temperature is far below the annealing temperature.

2.4 X-ray Diffraction

The spinel structure of all annealed samples was confirmed by X-ray diffraction patterns, which displayed characteristic spinel peaks and indicated the single-phase spinel structure. No additional phase was detected in any one of the samples. Diffraction peaks corresponding to different crystal planes of spinel cubic structure of all X-ray diffraction patterns were indexed by using the Debye-Scherrer method as well as with known planes of cubic spinel structure from the standard JCPDS cards of cobalt and zinc ferrites (JCPDS Card Nos. 89-1012, 22-1080 and 00-001-1121). The X-ray diffraction patterns of $Co_{1-x}Ni_xZn_{0.5}Fe_2O_4$ ($x = 0$ to 0.25 in steps of 0.05) are shown in Fig. 2.

Once the diffraction peaks were assigned to corresponding 2θ values, inter-planar distances were calculated using the Bragg law ($2d_{hkl}\sin\theta = n\lambda$) and they are in agreement with the reported values [8, 9]. The lattice parameter a has been calculated from each diffraction peak using the equation $a = d\sqrt{h^2 + k^2 + l^2}$ [10]. The lattice constant values obtained for higher angle peaks were extrapolated with the Nelson-Riley function $F(\theta) = \frac{1}{2}\left(\frac{\cos^2\theta}{\sin\theta} + \frac{\cos^2\theta}{\theta}\right)$ [11] in a graph for more accurate values of lattice parameter, and the corresponding plots are shown in Fig. 3. The lattice parameter for the base compound is in good agreement with the
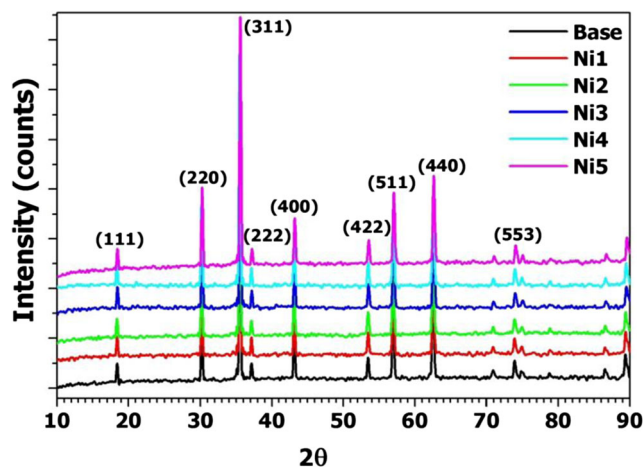
reported values [8, 9]. The inter-planar spacing(s) of different crystal planes and the lattice constants of the entire series of samples are shown in Table 1.

In the present series of samples, nickel is substituted in place of cobalt and both are different in magnetic nature; definitely, there would be changes in magnetic interactions. However, these two elements are successive in the periodic table; the difference in masses between them is very small. Furthermore, the cation radii of two ions are very close to each other; therefore, it is quite difficult to identify the changes except in some aspects. This proximity of cationic size in the present scenario is well displayed in d spacing(s), as there are few changes. In general, changes in d values are related to a shift glancing angle, 2θ. In turn, the peak angles are associated with changes in radius of the replaced ions as well as migration of cations over either sub-lattices or change in oxidation state or enhancements of grain diameters. The changes in d spacing(s) of particular plane indicate the preferential grain growth in the sample.

On a macroscopic observation of inter-planar spacing(s), which were observed to be constant for some planes, it was worth of investigating some of the micro-structural properties. On the whole, in nanomaterials, there are two types of strains observed in the crystal lattice: one is lattice strain and the other one is micro-strain [8]. Change in the surface tension produces lattice strain, which is displayed in the d spacing(s). Micro-strain occurs due to oxygen ion vacancies and crystal defects, which can be observed through peak broadening in X-ray diffraction pattern. Both were discussed in this section.

It is possible to observe lattice strain on crystallites when cobalt ions are replaced with nickel ions because of the change in d spacing(s) of all samples in the entire series, which may be realized using $(d - d_0 / d_0)$, where d_0 is the inter-planar spacing of the base sample, and the data is presented in Table 2. It is very much clear that Ni3 and

Fig. 3 Nelson-Riley plots of $Co_{1-x}Ni_xZn_{0.5}Fe_2O_4$ ($x = 0$ to 0.25 in steps of 0.05)
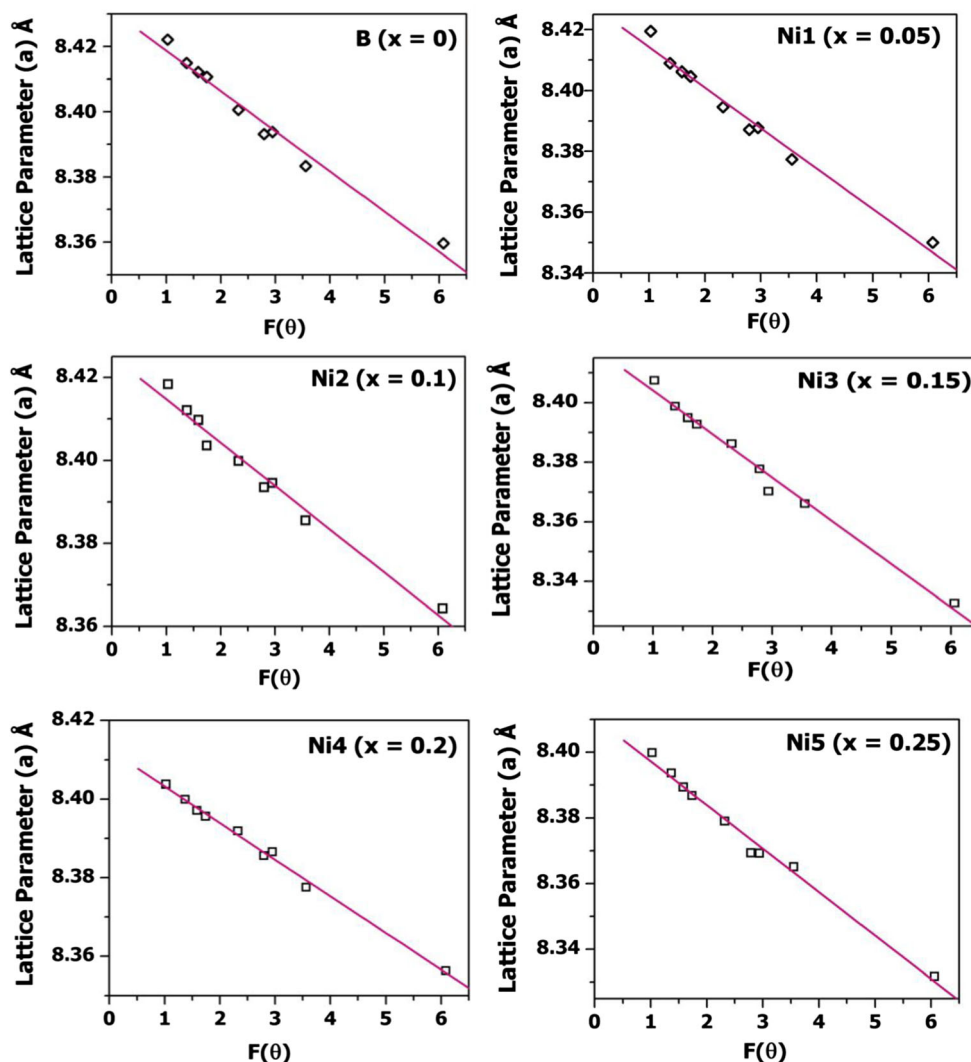
Ni5 are different by displaying positive lattice strain. On the other hand, Ni1, Ni2 and Ni4 displayed less as well as mixed variations in the strain values. These are well addressed

Table 1 Inter-planar spacing and lattice constant values of $Co_{0.5-x}Ni_xZn_{0.5}Fe_2O_4$

(hkl)	Sample					
	B	Ni2	Ni2	Ni3	Ni4	Ni5
(111)	4.8149	4.8128	4.8216	4.8040	4.8216	4.8040
(220)	2.9569	2.9602	2.9602	2.9536	2.9602	2.9536
(311)	2.5248	2.5248	2.5271	2.5201	2.5271	2.5201
(222)	2.4171	2.4193	2.4193	2.4150	2.4193	2.4128
(400)	2.0951	2.0967	2.0967	2.0936	2.0967	2.0920
(422)	1.7127	1.7137	1.7127	1.7107	1.7127	1.7097
(511)	1.6151	1.6159	1.6160	1.6133	1.6151	1.6124
(440)	1.4840	1.4848	1.4848	1.4826	1.4840	1.4818
(533)	1.2813	1.2818	1.2818	1.2803	1.2808	1.2793

in the next sections. It was noticed that the planes (222), (400) and (533) indicated the existence of strain. The reason for the discrepancy of lattice strain among different crystal planes is probably due to the greater stiffness of the sample in a specific direction. Furthermore, $\Delta d / d_0$ or $\Delta a / a_0$ is directly proportional to surface tension (γ). In solids, the surface tension is not compensated especially at the ends and the introduction of new ions into the system might bring force adjustments among all constituent ions. In other words, this might provide some useful explanation about the cation distribution as well as the magnetic properties. This tensile strain on nanoparticles leads to a decrease in lattice strain and almost constant inter-planar spacing.

While coming back to lattice constant, it displayed a decreasing trend with an increase in nickel concentration and it is attributed to the less cationic radius of substituted nickel (0.73 Å) to that of replaced cobalt (0.745 Å) ions [12]. The variation of lattice constant is in accordance with Vegards law, which supports the entry of nickel into

Table 2 Lattice strains of $Co_{0.5-x}Ni_xZn_{0.5}Fe_2O_4$ ($x = 0.05$ to 0.25)

(hkl)	Lattice strain $((d_0 - d) / d_0)$				
	Ni1	Ni2	Ni3	Ni4	Ni5
(111)	4.361×10^{-4}	-0.001	0.002	-0.001	0.002
(220)	-0.001	-0.001	0.001	-0.001	0.001
(311)	$-$	-9.11×10^{-4}	0.002	-9.11×10^{-4}	0.002
(222)	-9.102×10^{-4}	-9.102×10^{-4}	8.688×10^{-4}	-9.102×10^{-4}	0.002
(400)	-7.637×10^{-4}	-7.637×10^{-4}	7.16×10^{-4}	-7.637×10^{-4}	0.001
(422)	-5.839×10^{-4}	$-$	0.001	$-$	0.002
(511)	-4.953×10^{-4}	-5.572×10^{-4}	0.001	$-$	0.002
(440)	-5.391×10^{-4}	-5.391×10^{-4}	9.434×10^{-4}	$-$	0.001
(533)	-3.902×10^{-4}	-3.902×10^{-4}	7.805×10^{-4}	3.902×10^{-4}	0.002

spinel lattice. The last two samples (Ni3 and Ni5) showed a little deviation in lattice constant from the trend, which can be related to crystallite sizes and migration of cations between the sites, which is addressed in the next section. The obtained lattice constant of the base composition is in well agreement with the reported values, indicating the entering of all cations into the respective spinel lattices and formation of single-phase spinel structure. The variation in lattice constant with increasing in the nickel concentration of the present series is shown in Fig. 4.

In the present system, nickel is substituted in place of cobalt, so cation distribution cannot be obtained from Buerger's method as there is a very slight difference in scattering powers of these ions, since they are adjacent elements in the periodic table. However, it is possible to figure out the movement of cations between the two sub-lattices with the increase in nickel concentration from the intensities of (2 2 0) and (4 4 0) planes using X-ray diffraction data. Because these planes are more sensitive to the cations on tetrahedral and octahedral sites respectively the relative intensities of (2 2 0) and (4 4 0) planes with

reference to the most intense plane (311) are shown in Table 3. The differences between the relative intensities of these two planes might provide essential information regarding cation changes in both sites. Moreover, based on the available literature report(s), cobalt has a strong octahedral preference, whereas zinc has a strong tetrahedral preference [6, 9]. However, the introduction of nickel, which also has an octahedral site preference as cobalt, might be a possibility of migration of cations between the two sites.

It is apparent from Table 3 that the difference in the intensities of (2 2 0) and (4 4 0) planes is decreasing from the base sample to Ni4 ($x = 0.2$) and displayed the least value then increased in the last sample. The maximum difference was observed in the last sample similar to the base sample. In the base sample, cobalt ions occupied octahedral sites which were derived from Buerger's method and results were reported elsewhere [7]. Since the last sample displayed nearly the same value as the base, it may be concluded that cobalt ions occupied octahedral sites. In other words, it happened after a concentration of cobalt of 0.3 was obtained. Below this concentration, some cobalt ions had a chance to occupy tetrahedral sites as evident from the intensity differences. X-ray (theoretical) density values showed a decrease from the base to the last sample steadily, which are presented in Table 3.

2.5 Determination of Average Crystallite Size

After phase identification of nanoferrites, it is a tradition to determine crystallite size using the Scherrer equation, because of its simplicity in application and it also gives a preliminary idea about the crystallite size. In the Scherrer equation, the full width at half maximum (FWHM) of the most intense (311) peak was used to calculate crystallite size. In general, the profile fit of diffraction peak is observed to be Lorentzian or Gaussian or may be Voigt shaped. In the present series of nanoferrites, the shape of the profile fit of (311) diffraction peak was found to be Gaussian. Here, the
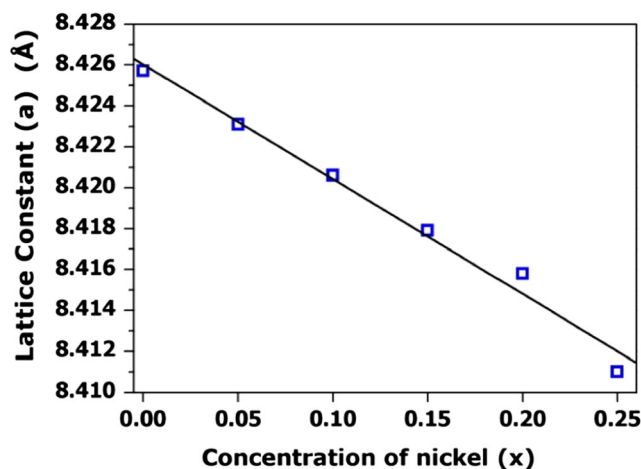

Fig. 4 Variation in lattice constant of $Co_{0.5-x}Ni_xZn_{0.5}Fe_2O_4$

Table 3 Intensities of crystal planes and X-ray densities of $Co_{0.5-x}Ni_xZn_{0.5}Fe_2O_4$

Sample	Relative intensity of (hkl) plane				$I(220) \sim I(440)$	$I(220)/I(440)$	X-ray density (g/cm³)
	(220)	(400)	(511)	(440)			
B	0.4665	0.5541	0.4815	0.4458	0.0207	0.9556	5.2991
Ni1	0.4363	0.5250	0.4524	0.4228	0.013501	0.9691	5.3037
Ni2	0.4086	0.4907	0.4249	0.3918	0.016791	0.9589	5.3081
Ni3	0.3904	0.4720	0.4209	0.3863	0.00408	0.9895	5.3129
Ni4	0.3716	0.4532	0.3996	0.3683	0.003282	0.9911	5.3166
Ni5	0.3622	0.4272	0.3732	0.3375	0.024686	0.9318	5.3255

crystallite sizes (D) of all samples were obtained using the Scherrer equation, $D = k / \beta \cos\theta$, where k is the Scherrer or shape factor (the Gaussian limit for the shape factor is 0.9394 [13]), θ is the Bragg angle, λ is the wavelength of X-rays (1.5406 Å) and β is the broadening of diffraction peak. The contribution of instrumental broadening (β_0) was removed using Warren's formula $\beta = \beta_e - \beta_0$ where β_e is the FWHM of the diffraction peak in radians. As such, the obtained crystallite sizes were observed to be in the range of 34–37 nm.

However, these values may not be accurate as there might another possibility of peak broadening due to lattice strain, which was not taken into consideration. As the Scherrer formula undoubtedly given to confirm the presence of nanocrystallites in the samples, the Williamson-Hall (W-H) plot was used to fine tune the crystallite size. This method, in which size broadening of the peak is only considered for crystallite size determination, is a special feature of the W-H method. As such, the crystallite size of the samples and their strain or lattice distortion are believed to be the reasons for the broadening of X-ray diffraction peak; mathematically, this relation can be expressed as [13]
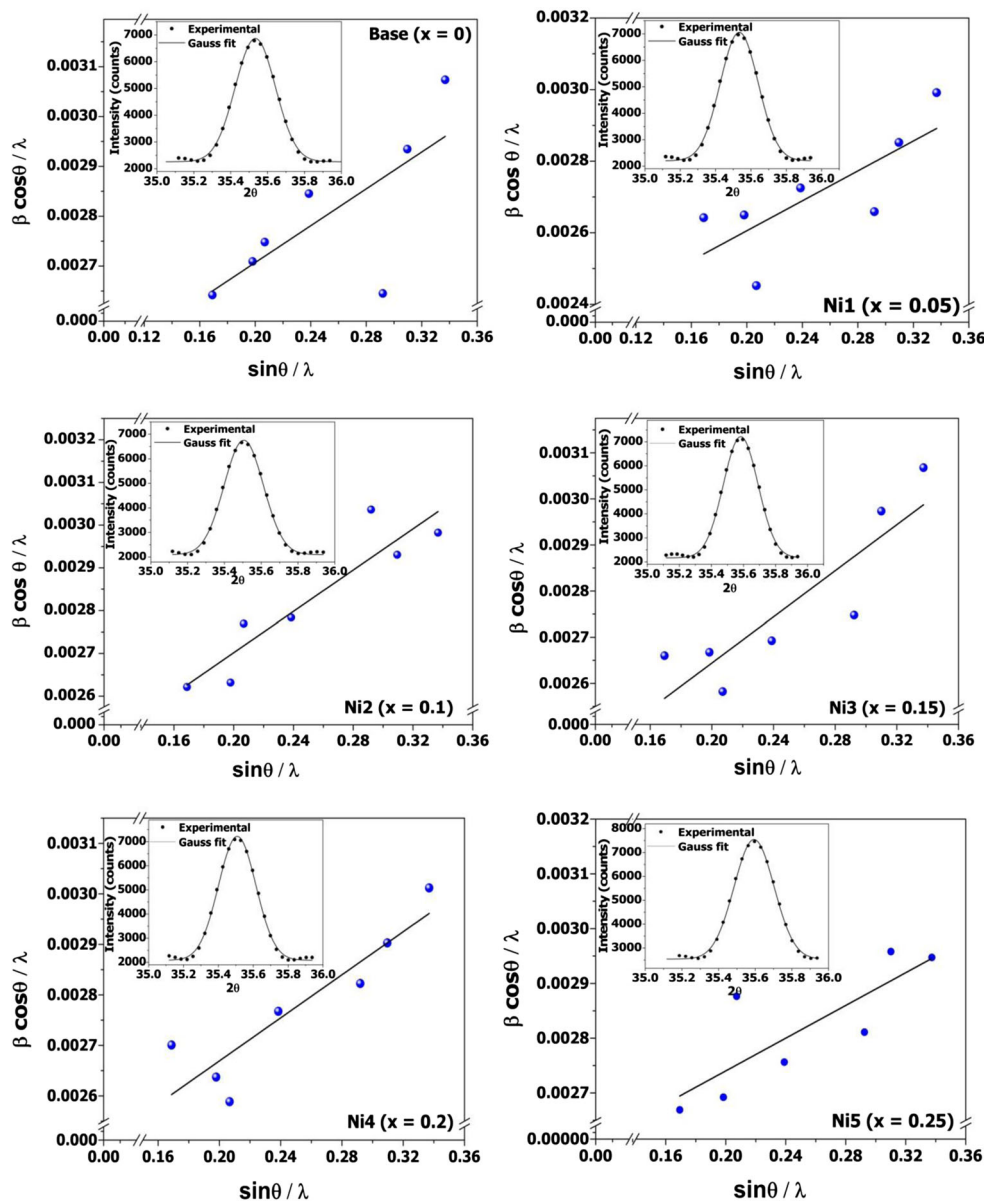
$$\beta = \beta_{size} + \beta_{strain}$$

In practice, this equation can be expressed as $\frac{\beta \cos\theta}{\lambda} = \frac{k}{D} + \frac{4\varepsilon \sin\theta}{\lambda}$, where β is the FWHM of the diffraction peak, β_{size} is the FWHM due to the effect of crystallite size only, β_{strain} is the FWHM due to the effect of micro-strain only, D is the crystallite size (nm), k is the shape factor, ε is the lattice strain, θ is the incident angle of the X-ray and λ is the wavelength of X-ray beam (1.5406 Å).

This relation clearly separates the contributions from crystallite size and micro-strain by fitting the experimentally observed diffraction peak data. A plot of $\beta \cos\theta / \lambda$ versus $\sin\theta / \lambda$ (Williamson-Hall plot) can clearly isolate the effects of size and strain broadenings from each other. The horizontal line of the graph represents significant size

broadening. On the other hand, strain broadening is also considered to be an important contribution if the plot is a linear function of $\sin\theta$. The latter is most common in nanomaterials. Williamson-Hall plots for all samples were drawn, and the average crystallite size was calculated from the y-intercept of the plots by making the strain component zero. The crystallite sizes obtained from the W-H plots were slightly higher than those obtained from the (311) peak alone. This indicates the possibility of a mixed range of crystallites with a size difference of 2–5 nm. The profiles of (311) peak after curve fitting along with the W-H plots of all samples are shown in Fig 5. All plots indicated the existence of micro-strain as there is an increase in the linear fit. Micro-strain is a quantitative indication of the presence of anion/cation vacancies and crystal defects. In the present series of samples, a very small value of micro-strain indicates filling of O^{2-} vacancies on annealing in air (oxygen) atmosphere. The samples Ni2, Ni3 and Ni4 displayed slightly high micro-strain when compared to the rest of the samples. This might provide an insight to magnetization values which will be discussed in the final section. Although the W-H plot gives a reliable crystallite size, the goodness of fit in the plot (coefficient R of linear fit) is also important. The range of R values was observed to be from 0.71 to 0.97 for all W-H plots. These values of correlation coefficients of linear fits in W-H plots are in the threshold as well as in permissible range as the W-H plot method is very much suitable for a crystallite size of more than 20 nm. On the other hand, the R values or the goodness of fit clearly shows the accuracy of the crystallite size and the values could be further improved to achieve a value very near to 1 (ideal values of R). Therefore, these values can be further correlated to the TEM measurements regarding particle size. This can be made possible by adapting a better method called size-strain analysis, in which the FWHM of lower-angle as well as higher-angle peaks in diffraction pattern was also given equal importance. The crystallite size and the strain values of all samples are presented in Table 4.

Fig. 5 W-H plots of $Co_{0.5-x}Ni_xZn_{0.5}Fe_2O_4$

The broadening of diffraction peaks in the size-strain (S-S) plot method [13] can be expressed as

$$\beta_{hkl}^2 = \beta_{size}^2 + \beta_{strain}^2$$

Inter-planar distance is a part of this relation, and the complete equation can be expressed as

$$(d_{hkl}\beta_{hkl}\cos\theta)^2/\lambda^2 = (k/D)(d_{hkl}^2\beta_{hkl}\cos\theta)/\lambda) + \left(\frac{\Sigma}{2}\right)^2$$

where $\Sigma = x(2(2\pi)^{1/2})\varepsilon$.

In this method, convolution of the crystallite of size and strain contributions can be made easily by plotting $(d_{hkl}\beta_{hkl}\cos\theta)^2/\lambda^2$ versus $d_{hkl}^2\beta_{hkl}\cos\theta)/\lambda$. These plots are referred as size-strain plots (S-S plots), and they were drawn for all current series of nanoferrites; the average crystallite size was calculated from the slope of the linear fit and micro-strain is calculated from the y-intercept of the plots. This method is treated to be the best for evaluating the smaller crystallite sizes of the nanomaterials. However, the crystallite size(s) obtained from both the Scherrer formula and W-H plot indicated moderate value(s). The correlation coefficients of the fit (R values) were very close to 1, showing the goodness of fit even at narrow size distribution of 2–5 nm as discussed above. The size-strain plots of all samples are shown in Fig. 6.

Table 4 Crystallite size and lattice strains of $Co_{1-x}Ni_xZn_{0.5}Fe_2O_4$ ($0 \leq x \leq 0.25$, $x = 0.05$)

Sample	Crystallite size (nm)			Strain		Correlation coefficient (R)	
	Scherrer equation	W-H plot	S-S plot	W-H plot ($\times 10^{-4}$)	S-S plot ($\times 10^{-4}$)	W-H plot	S-S plot
B	34.71	40.1	37.89	6.1	3.82	0.9708	0.9985
Ni1	35.94	42.9	37	6.71	4.6	0.7164	0.9944
Ni2	34.54	42.3	35.5	7.51	5.05	0.9104	0.9964
Ni3	37.56	43.9	36.6	7.73	5.1	0.8547	0.9960
Ni4	36.50	41.9	36.5	6.81	5.14	0.9059	0.9969
Ni5	36.66	38.5	34.2	5.21	3.28	0.8132	0.9979

The crystallite sizes as well as micro-strain of all samples obtained in this method were observed to be slightly less than the values obtained in the W-H plot method. But, both showed the same positive sign, an indication of lattice expansion. The substituted nickel is smaller than the replaced cobalt and the contraction of the lattice is expected. But after the annealing process, the crystallite size is increased by nearly 10 nm. These details of the as-prepared base sample are published elsewhere [7]. All the samples showed positive micro-strain or, in other words, tensile strain, indicating the expansion of the lattice, which is evident after the annealing process which results in the growth of crystallites.

Fig. 6 Size-strain (S-S) plots of $Co_{1-x}Ni_xZn_{0.5}Fe_2O_4$ ($0 \leq x \leq 0.25$, $x = 0.05$)
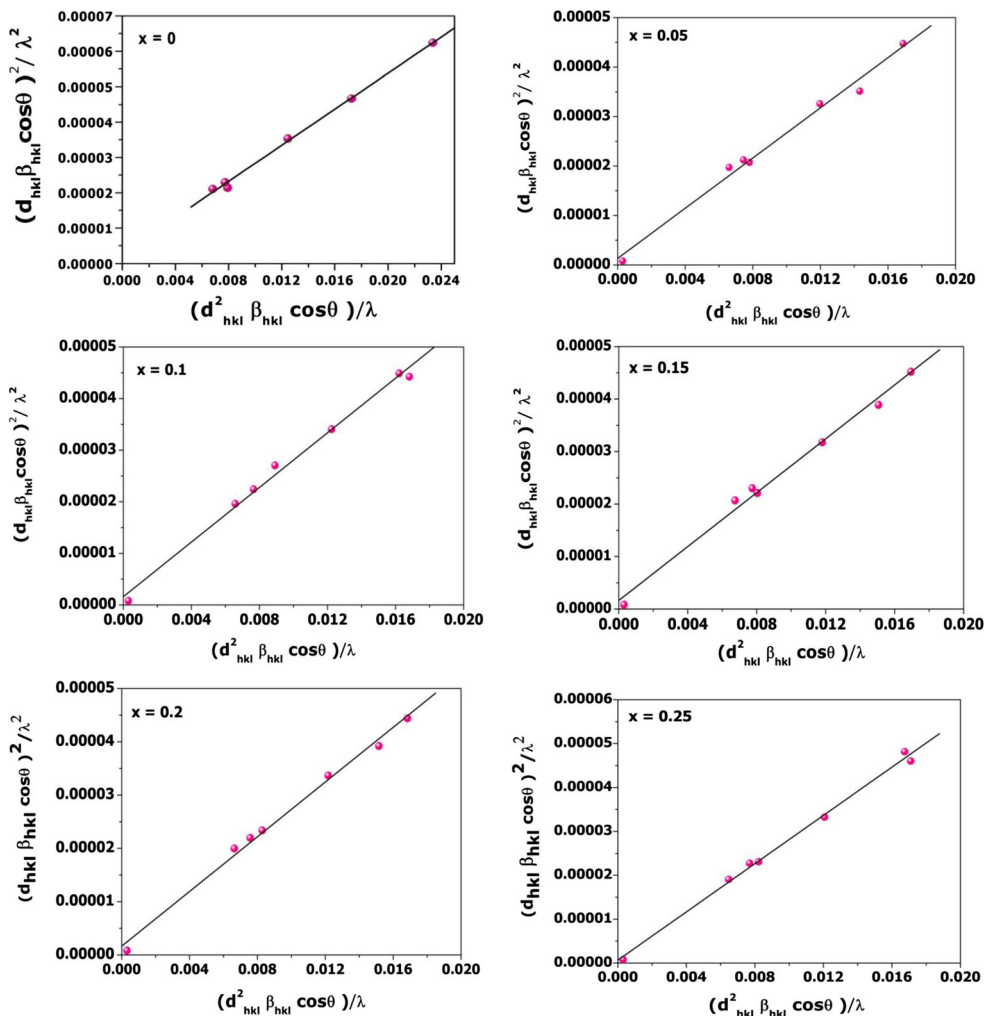
2.6 Morphological Studies and EDX Analysis of Base ($x = 0$)

TEM image(s) of the base indicates the spherical morphology, and average particle size was about 35.1 nm. There were few reports available with $\pm 10\%$ deviation, and this can be attributed to the conditions employed during the synthesis [8, 9]. However, in the other TEM images of different resolutions, there were several fine particles ranging from 4 to 9 nm and very rare above 50 nm, which was supported by a selected area electron diffraction (SAED) pattern, which displayed diffused rings. This ring clearly demonstrates the existence of fine/nanoparticles. The particle size reported here is less than a reported value(s) for the same composition [14]. The TEM micrograph and SAED pattern of the base ($x = 0$) are shown Fig. 7.

The base ($x = 0$) sample was examined through scanning electron microscopy for surface and morphology study, and it is shown in Fig. 8. The investigation reveals the well-formed grains with different sizes. The sample displayed poor grain structure with different grain diameters, among them small grains are relatively high and also grain boundaries were not clear. The average grain size was calculated using a linear intercept method, and the average grain size was observed to be 121 nm. In substituted cobalt ferrites, the presence of cobalt at high concentrations of ferromagnetic cobalt ions may result in having permanent dipole moment which leads to agglomeration, giving rise to poor grain formation.

In actual fact, there was a noticeable difference in the crystallite size/particle size as calculated from XRD and TEM with these SEM grain size values. It is a known fact that the resolution of SEM is not effective to clearly differentiate particles, but it can give the grain growth with dopant/substituent concentration. Furthermore, the intensity of the XRD is proportional to the square of the volume or, in other words, the measured size is the result of an average
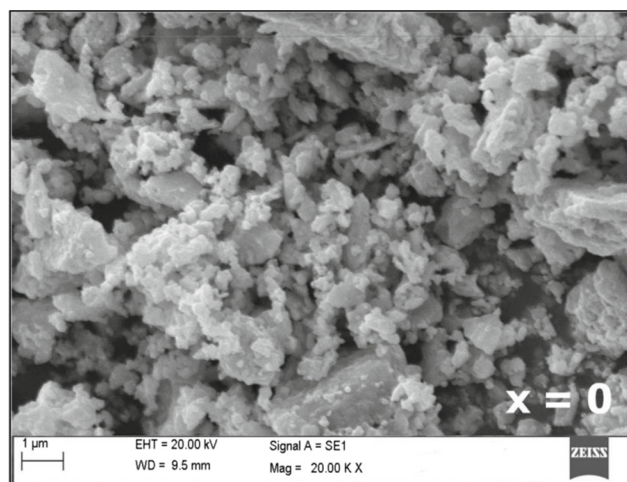

Fig. 8 SEM micrograph of $Co_{0.5}Zn_{0.5}Fe_2O_4$

weighed by a six power of the crystal radius. Therefore, the signals are having variable intensity with diameters of particles, which depends on sample dispersion. As a result, the size measured from XRD peaks should always be smaller than the one obtained by electron microscopy [15]. Further, the stoichiometric proportion of elements/ions was confirmed by EDX analysis. The analysis was performed at a working distance less than 10 mm to make sure the scattering electrons were well captured. The chemical composition of the base compound is nearly the same according to the percentages of atoms as per EDX spectrum. The EDX spectrum of the base (B) is presented in Fig. 9, and the corresponding percentages of the constituent elements are presented in Table 5.

The spectra confirmed the presence of Co, Zn, Fe and O atoms. There were no additional elements/impurities detected in these samples. From Table 5, it is very much clear that the base sample displayed nearly equal percentages of elements as per the chemical composition and are nearly balanced

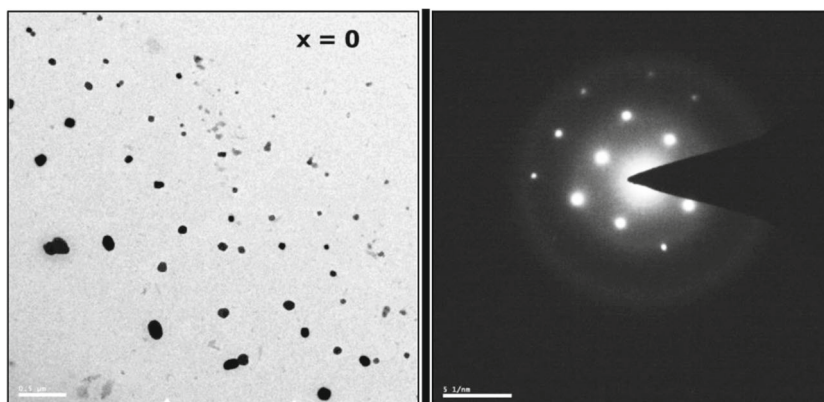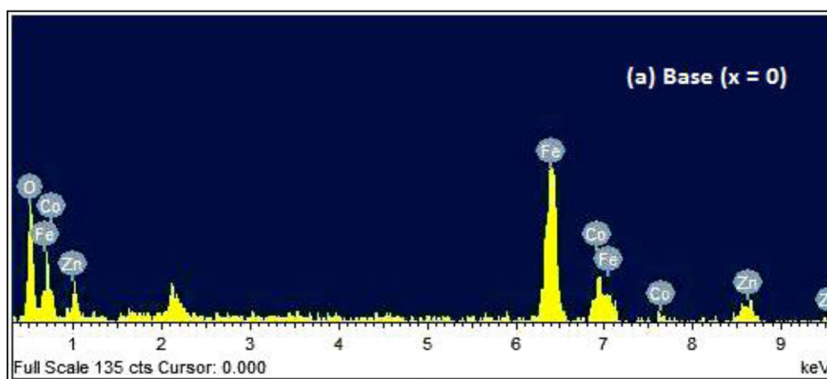**Fig. 7** TEM micrograph and SAED pattern of base ($x = 0$)

Fig. 9 EDX spectrum of $Co_{0.5}Zn_{0.5}Fe_2O_4$

with the metal cation-to-anion ratio 3:4. The observed very slight variation is due to few oxygen ion vacancies, and the composition contains four types of atoms. The detection of atoms in EDX (or EDAX or EDS) is based on the mass of the atoms. Since Co, Zn and Fe have comparable masses so the percentages can be thought of exact numbers, the presence of oxygen in the system which has less mass compared to the individual masses of all atoms in the system can be observed; thus, the percentages might have ±2 variation.

2.7 Far IR Study

Far IR spectra were recorded at room temperature for all samples in the active absorption region of spinel ferrites (100–800 cm^{-1}). Specifically in nanoregime, the position of absorption bands in the active region of infrared spectrum is strongly dependent on the composition of the ferrite, method of preparation, size the particles/grains, cation radii and atomic mass. These characteristic bands are lattice vibrations and strongly depend on any structural changes brought about by a substituent or incorporated metal cation. These types of atomic displacements (T_2, E) are due to the bond bending and bond stretching so that in general, $\upsilon(T_2) < \upsilon(E)$. Change in dipole moment due to the bond stretch (symmetric and asymmetric) produces υ_1 and υ_2 absorption bands. Change in dipole moment due to the bond bending produces υ_3 and υ_4. The sequence of the absorption

bands is given by the following expression for any ferrite system whether it is normal, mixed or inverse: $\upsilon_4(T^t) < \upsilon_3(T^{t/o}) < \upsilon_2(E^o) < \upsilon_1(E^t)$. Out of these four, the υ_4 band frequency depends on the mass of the tetrahedral cation and is assigned to some type of vibrations involving tetrahedral metal ions. However, the site symmetry of the metal complex and the site preference of the divalent metal cation influence the band υ_3 in a mixed or inverse ferrite; as such, υ_3 is considered to be from octahedral metal complex [5]. The far IR spectrum of all samples is shown in Fig. 10.

All samples clearly showed four characteristic absorption bands in the range of 260–560 cm^{-1}, which is very near agreement to the reported values for the base composition [9]. Four characteristic IR absorption bands of all current series samples are shown in Table 6. However, there were few shoulder absorption bands to these fundamental bands. Among four absorption bands of all samples, there were slight changes in band positions except for a few. These were attributed to the possible presence of different metal cations at a particular site. The differences in peak width as well as the absorbance were also accounted for these changes. In the fourth absorption band, the band positions were almost constant which was due to very

Table 5 Weight percentages of individual ions in $Co_{0.5}Zn_{0.5}Fe_2O_4$

Element	Base	
	Weight %	Atomic %
O (K)	26.005	56.005
Fe (K)	47.168	29.11
Co (K)	12.953	7.575
Zn (K)	13.874	7.31
Total	100	100
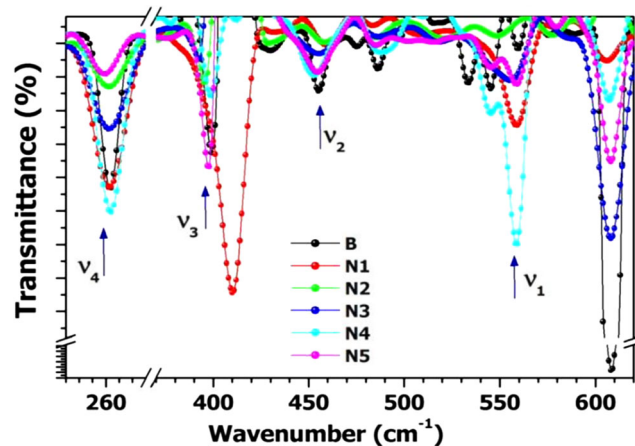
Fig. 10 Far IR spectrum of $Co_{1-x}Ni_xZn_{0.5}Fe_2O_4$ ($0 \leq x \leq 0.25$, $x = 0.05$)

Table 6 Positions of the absorption bands of $Co_{1-x}Ni_xZn_{0.5}Fe_2O_4$ ($0 \leq x \leq 0.25$, $x = 0.05$)

| Sample	Position of the absorption band (cm^{-1})			
	υ_1	υ_2	υ_3	υ_4
B	546	455	399	262
Ni1	559	459	410	261
Ni2	548	459	395	261
Ni3	556	455	–	261
Ni4	559	452	399	262
Ni5	558	454	398	260

close atomic masses (Ni 58.693, Co 58.933). The high intensities also reflect the strength of Fe^{3+}–O^{2-} bonds at tetrahedral and octahedral sites, since the motions involved are predominantly those of the oxygen ion. These effects are also shown in saturation magnetization, which is discussed in the next section.

2.8 Magnetic Measurements

In general, the magnetization of spinel ferrites is strongly affected with the change in super-exchange interactions between A and B site cations, dia/para/ferromagnetic nature of cations, distribution of cations between A and B sites, bond lengths, particle/grain size and angles (radii of the cations). As a whole, Neel's two sub-lattice model is used to explain the magnetization behaviour of spinel ferrites. This model describes the magnetization of a ferrite material as the difference between net magnetizations of two sub-lattices (octahedral and tetrahedral sites) in the unit cell aligned anti-parallel to each other. This model is applicable to good crystalline ferrite materials with less lattice distortion, which is due to change in symmetry of octahedral site. In such a case where the substituted cation in the ferrite system is capable of introducing John-Teller distortion, three sub-lattice model is considered to be the best since it was based on the spin canting effects, i.e. the deviation of anti-parallel alignment of tetrahedral and octahedral sites as well as the inclined alignment of spins in octahedral sites. Magnetization curves of the current series of samples were recorded at room temperature in the range about 0–15 kOe. The M-H loops of all samples recorded at room temperature are presented in Fig. 11, and all magnetic parameters are shown in Table 7.

The magnetic parameters collected from the M-H curves are presented in Table 7. The base sample displayed a saturation magnetization of 50.2 emu/g. This is small compared to the same composition reported in the literature, this is related to lower crystallite size and it is evident from the TEM micrographs. The particle size is 15% smaller
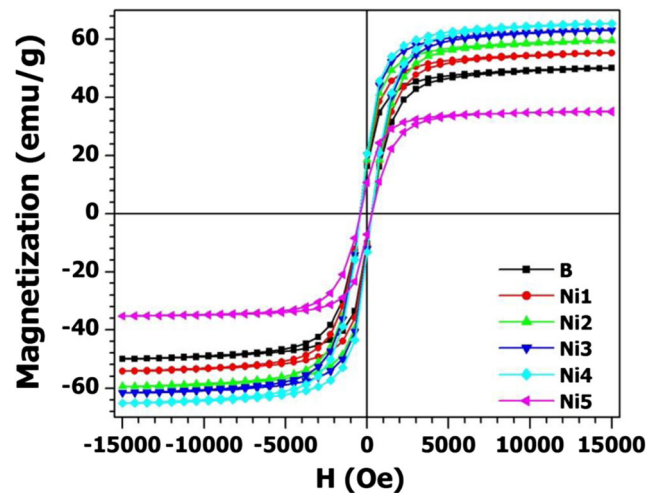
Fig. 11 Magnetization curves of $Co_{0.5-x}Zn_{0.5}Ni_xFe_2O_4$ ($x = 0$ to $x = 0.25$) at room temperature

than those reported in the literature [14]. Based on the magnetization of the base, its cation distribution can be expressed as

$$(Zn_{0.5}Fe_{0.5})[Co_{0.5}Fe_{1.5}]O_4$$

This cation distribution was confirmed using Buerger's method using the intensities of X-ray diffraction peaks. The introduction of divalent and weak ferromagnetic nickel ions (2 μ_B) in place of cobalt into the system may slightly reduce magnetization values. But, in the present case, the magnetization initially increased up to $x = 0.2$, and later it decreases. This can be explained on the basis of the octahedral preference of cations in the system. It is well known that ferromagnetic Fe^{3+} (5 μ_B) occupies both tetrahedral and octahedral sites. The concentration of these Fe^{3+} ions at respective sub-lattice changes with the concentration and movement of divalent cations. In addition to Fe^{3+} ions, the current system under consideration has diamagnetic divalent zinc ions (0 μ_B), ferromagnetic Co^{2+} ions (3 μ_B) and weak ferromagnetic Ni^{2+} ions (2 μ_B). Among these, it is well established that zinc ions occupy tetrahedral sites and it was also confirmed from the base cation distribution. On the other hand, the cobalt and nickel ions both have preferential octahedral site occupancy. However, cobalt has a small tetrahedral site preference but it depends on the other cations in the system. Since the crystal field stabilization energy of nickel is greater than cobalt, it is obvious that the introduction of nickel ions into the octahedral site makes few concentrations of cobalt ion to occupy tetrahedral sites. This would result in migration of iron ions from tetrahedral to octahedral sites, which leads its increase in magnetization, thereby increasing the net magnetization of the system. Similar behaviour is reported in cobalt and nickel containing ferrite

Table 7 Saturation magnetization, coercivity, remanence, squareness ratio, experimental and theoretical Bohr magnetons of samples $Co_{0.5-x}Zn_{0.5}Ni_xFe_2O_4$ ($x = 0$ to $x = 0.25$)

Sample	Saturation magnetization (emu/g)	Molecular weight (amu)	Experimental Bohr magnetons (μ_B)	Coercivity (Oe)	Remanence (emu/g)	Squareness ratio
B	50.2	237.8587	2.14	361	13.29	0.2647
Ni1	55.42	237.8467	2.36	361.5	14.5	0.2616
Ni2	59.59	237.8347	2.54	362	15	0.2517
Ni3	63.33	237.8227	2.70	360.5	16	0.2724
Ni4	65.68	237.8107	2.80	357.5	17.25	0.2741
Ni5	35.3	237.7988	1.50	360	9	0.2550

systems. In this scenario, Ni4 ($x = 0.2$) displayed the highest magnetization of all samples with 65 emu/g. The occupancy cobalt into tetrahedral sites was continued up to an optimal concentration level of cobalt ions (0.3). After this concentration, nickel and cobalt both co-existed in octahedral sites, thus decreasing the magnetization as a whole. It was observed in the last sample Ni5 ($x = 0.25$). Moreover, the smaller crystallite size of Ni5 of all samples was also a reason for this least magnetization (35.5 emu/g) of the entire series.

The saturation magnetization of all samples followed exact synchronization with micro-strain (Fig. 12). Deviations from the ideal lattice arrangement cause local changes of the electronic band structure, which modifies the magnetic anisotropy of a given material through spin-orbit coupling. The highest value of saturation magnetization was observed for Ni4 sample, and also, it displayed the highest micro-strain.

Experimental Bohr magnetons at room temperature per one formula unit are calculated from the following relation [10]:

$$n_B = (M_{wt} \cdot M_s)/5585$$

where M_{wt} is the molecular weight and M_s is the saturation magnetization.
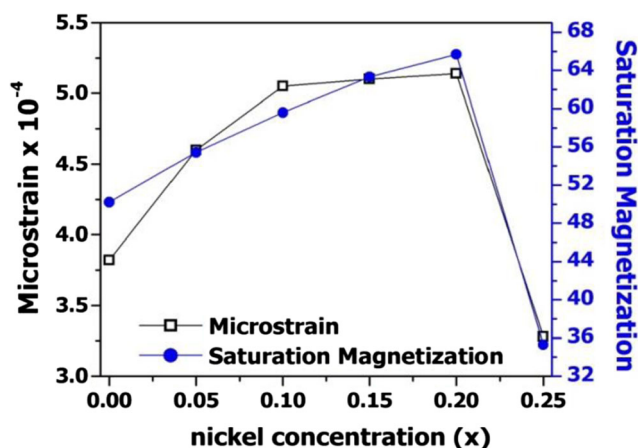

Fig. 12 Saturation magnetization and micro-strain versus nickel concentration

The saturation magnetization of all samples exactly followed the trend of intensity ratios obtained from room-temperature X-ray diffraction patterns. This clearly demonstrates that the cation distribution proposed from X-ray diffraction study holds for magnetic properties also. The experimentally observed intensity ratios of planes which are sensitive to tetrahedral and octahedral sites along with saturation magnetization of the entire series of samples were in direct correlation with each other. It is clear that the variation in saturation magnetization followed the intensity ratio $I(440)/I(220)$ in opposite trend, and intensity values are displayed in Table 3. The above-mentioned reasons for the variation in saturation magnetization with nickel concentration are well acceptable. The anisotropic nature of magnetization produces a tilt angle away of the average magnetization from the normal direction. This can be understood by considering the ratio between remanent and saturation magnetization. It was surprising that the reduction in cobalt ions at octahedral sites should lead to a decrease in anisotropy; however, the increase in magnetization due to stronger A-B interactions balanced the overall anisotropy. Therefore, all remanence ratios were nearly the same. The coercivity was observed to be constant throughout the series except in Ni4, where it was slightly less. This might be due to the highest magnetization. The decrease in reduction in cobalt at octahedral sites might be able to trim down coercivity, but the increase in saturation was able to control these values so that the coercivity remained nearly constant throughout the series.

The interaction between the uncompensated orbital magnetic moment of cobalt ions due to its typical $3d$ shell occupancy and the lattice leads to magnetocrystalline anisotropy in cobalt-containing ferrites. This effect is predominant when cobalt ions occupy octahedral sites. In cobalt ions at octahedral sites, the crystalline field is not able to quench the orbital magnetic moment; thus, it interacts with spin magnetic moments resulting in L-S coupling and these ions situated on a threefold axis of symmetry; it has four hard directions parallel to the body diagonals, and they are represented by [111], [$\bar{1}$11], [1$\bar{1}$1] and [$\bar{1}\bar{1}$1]. It also has six easy directions of magnetization along [111]

and 12 saddle points across the face diagonals [16]. Since, the orbital magnetic moment is so strongly attached to the lattice in such way that both contributions are significant. As such, magnetocrystalline anisotropy is very high in these ferrites.

With the objective of evaluating magnetocrystalline anisotropy constant (MAC), it must be remembered that the size and structural parameters would be important as they strongly influence MAC. In the present series of samples, a change in magnetocrystalline anisotropy is expected since strong paramagnetic nickel replaces ferromagnetic cobalt ions. MACs for all samples were determined using the law of approach (LA) to saturation over magnetization, which can be represented as $M = M_s[1 - \frac{b}{H^2}] + kH$ [17], where the term kH is called forced magnetization, $b = (8/105)(K_1^2 / \mu_0^2 M_s^2)$, H is the applied magnetic field and M_s is the saturation magnetization. In the present

situation, M-H loops were recorded at room temperature so the term kH was neglected since it plays a role at high temperatures and fields. Thus, $M = M_s[1 - \frac{b}{H^2}]$ can be used for evaluating anisotropy constant (K_1), by plotting graphs with M versus $\frac{1}{H^2}$ and they are shown in Fig. 13. This plot gives a linear fit, and the intercept on the y-axis represents M_s and from the slope of the graph, b can be obtained. Based on the relation mentioned above, K_1 is calculated from the value of b.

The anisotropy constant (K_1) was linearly increased from the base sample and reached to the highest value at Ni4 ($x = 0.2$). It was anticipated that cobalt concentration at B site decreases the magnetocrystalline anisotropy constant; nonetheless, the values displayed almost opposite trend except the last sample Ni5. This is mainly due to the change in bond angles and lengths, as well as the increase in saturation magnetization along with larger grains. The

Fig. 13 Law of approach to saturation of $Co_{0.5-x}Zn_{0.5}Ni_xFe_2O_4$ ($x = 0$ to $x = 0.25$) at room temperature

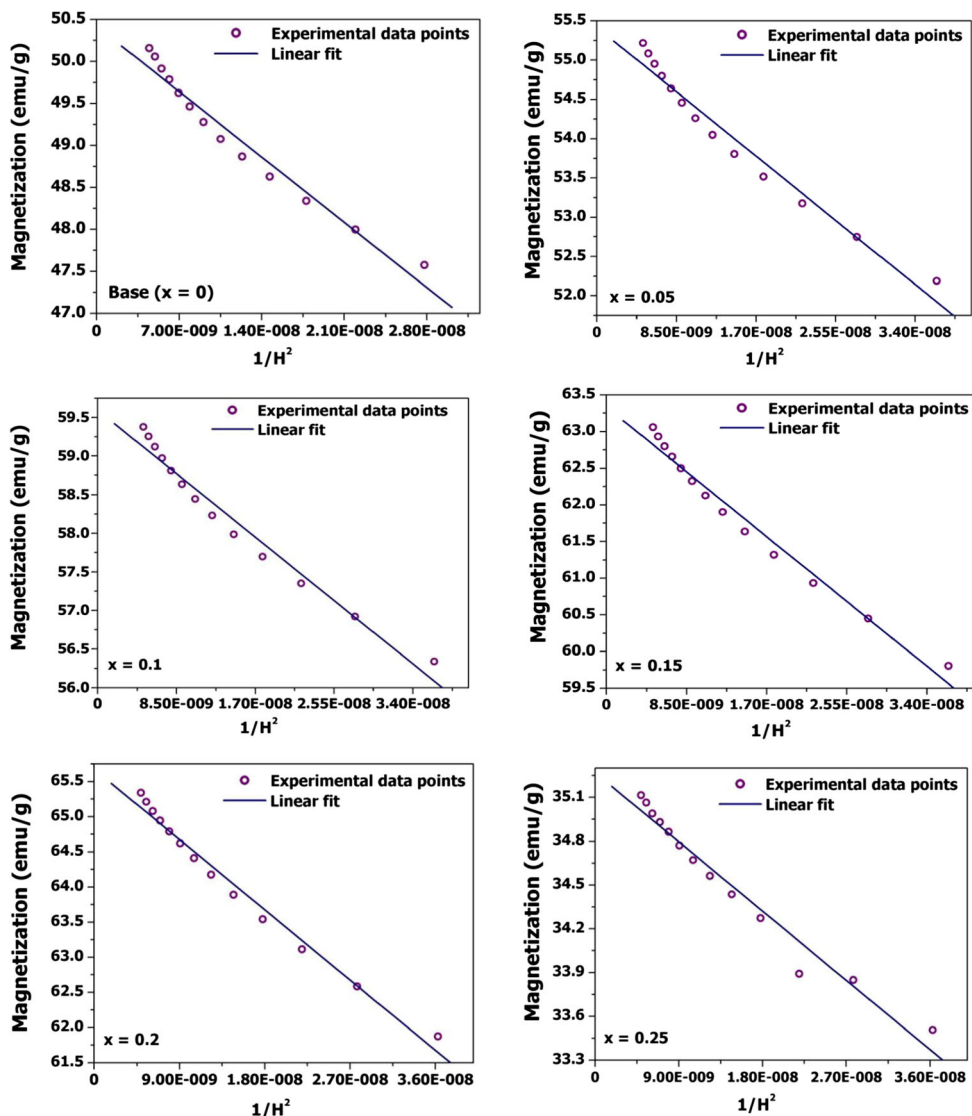**Table 8** Magnetocrystalline anisotropy constant and anisotropy fields of samples $Co_{1-x}Ni_xZn_{0.5}Fe_2O_4$ ($x = 0$ to $x = 0.25$)

Sample	Anisotropy constant ($\times 10^6$; erg/g)	Anisotropy field (kOe)
B	1.92	76.37
Ni	1.97	71.1
Ni2	2.12	71.2
Ni3	2.34	73.9
Ni4	2.51	76.4
Ni5	0.93	52.6

magnetocrystalline anisotropy of a ferrite system is helpful in the sustainability of magnetic ordering and for the display of ferromagnetic behaviour, which is crucial for data storage applications. Additionally, anisotropy constant and anisotropy field are key requirements for the determination of cut-off frequency in specific power applications [6]. Anisotropy field is calculated using $H_K = 2K_1/\mu_0 M_s$ [18], and the values of anisotropy fields were above 50 kOe for the entire series of samples. Based on all magnetic parameters such as saturation magnetization, coercivity, squareness ratio and magnetocrystalline anisotropy, the present series of nickel-substituted cobalt zinc nanoferrites showed better characteristics compared to reported cobalt zinc and substituted nanoferrite systems [6, 8, 9, 14] in view of data storage and power applications. The values of magnetocrystalline anisotropy constant and anisotropy fields are shown in Table 8.

3 Conclusions

Nanocrystalline $Co_{1-x}Ni_xZn_{0.5}Fe_2O_4$ ($x = 0$ to $x = 0.25$) was successfully synthesized using the citrate gel auto-combustion method. XRD patterns of all samples revealed single-phase spinel structure. DTA analysis was performed to record ferritization temperatures. Lattice parameter showed a decreasing trend and attributed to the small ionic difference between substituted nickel ions over replaced cobalt ions at B sites. The crystallite size(s) from XRD peaks showed the range of 34–38 nm from the Scherrer equation. These values were well refined using the W-H plot and S-S plot. TEM measurements indicated the presence of fine particles in the base sample with an average particle size of 35 nm. Far IR displayed characteristic absorption bonds. SEM micrograph of the base sample indicated mixed grains as well as near-spherical grains. EDX measurements revealed the presence of stoichiometric proportions of individual ions in the base sample. Saturation magnetization values showed an increase from 50.2 emu/g of base to 65 emu/g of Ni4 ($x = 0.2$), then followed

by an abrupt decrease to 35 emu/g of Ni5 ($x = 0.25$). Coercivity was changed slightly, an overall change of 4 Oe for the entire series was observed and squareness ratios were observed to be almost constant.

References

1. Yadav, R.S., et al.: Magnetic properties of $Co_{1-x}Zn_xFe_2O_4$ spinel ferrite nanoparticles synthesized by starch-assisted sol–gel auto combustion method and its ball milling. J. Magn. Magn. Mater. **378**(15), 190–199 (2015)
2. Kotsikau, D., et al.: Structure and magnetic properties of manganese zinc-ferrites prepared by spray pyrolysis method. Solid State Sci. **39**, 69–73 (2015)
3. Akhtar, M.N., et al.: Evaluation of structural, morphological and magnetic properties of CuZnNi ($Cu_xZn_{0.5-x}Ni_{0.5}Fe_2O_4$) nanocrystalline ferrites for core, switching and MLCI's applications. J. Magn. Magn. Mater. **421**(1), 260–268 (2017)
4. Ashiq, M.N., et al.: Role of Co–Cr substitution on the structural, electrical and magnetic properties of nickel nano-ferrites synthesized by the chemical co-precipitation method. Mater. Res. Bull. **47**(3), 683–686 and references therein (2012)
5. Vara Prasad, B.B.V.S., Ramesh, K.V., Srinivas, A.: Structural and magnetic studies of nano-crystalline ferrites MFe_2O_4 (M = Zn, Ni, Cu, and Co) synthesized via citrate gel auto-combustion method. J. Supercond. Nov. Magn. (2017). https://doi.org/10.1007/s10948-017-4153-y
6. Fiorillo, F.: Anisotropy and magnetization process in soft magnets: principles, experiments, applications. J. Magn. Magn. Mater. **304**, 139–144 (2006)
7. Vara Prasad, B.B.V.S., Ramesh, K.V., Srinivas, A.: Structural and magnetic studies on Co-Zn nanoferrite synthesized via sol-gel and combustion methods. Mater. Sci-Pol. accepted (2017)
8. Raut, A.V., Barkule, R.S., Shengule, D.R., Jadhav, K.: Synthesis, structural investigation and magnetic properties of Zn^{2+} substituted cobalt ferrite nano particles prepared by the sol–gel auto-combustion technique. J. Magn. Magn Mater. **358–359**, 87–92 (2014)
9. Singhal, S., Sharma, R., et al.: Structural, electrical and magnetic properties of $Co_{0.5}Zn_{0.5}Al_xFe_{2-x}O_4$ (x = 0, 0.2, 0.4, 0.6, 0.8 and 1.0) prepared via sol–gel route. Ceram. Int. **38**, 2773–2778 (2012)
10. Sivaram Prasad, M., Prasad, B.B.V.S.V., Rajesh, B.B., Rao, K.H., Ramesh, K.V.: Magnetic properties and DC electrical resistivity studies on cadmium substituted nickel–zinc ferrite system. J. Magn. Magn. Mater. **323**(16), 2115–2121 (2011)
11. Vara Prasad, B.B.V.S., et al.: Structural and dielectric studies of mg^{2+} substituted Ni–Zn ferrite. Mater. Sci-Poland **33**(4), 806–815 (2015)
12. Shannon, R.D.: Revised effective ionic radii and systematic studies of interatomic distances in halides and chalcogenides. Acta Crystallogr. A **32**, 751–767 (1976)
13. Maniammal, K., Madhu, G., Bijua, V.: X-ray diffraction line profile analysis of nano structured nickel oxide: shape factor and convolution of crystallite size and micro-strain contributions. Phys. E. **85**, 214–222 (2017)
14. Deraz, N.M., Alarifi, A.: Structural, morphological and magnetic properties of nano-crystalline zinc substituted cobalt ferrite system. J. Anal. Appl. Pyrolysis **94**, 41–47 (2012)

15. Rana, K., Thakur, P., Arul Sharma, P., Tomar, M., Gupta, V., Thakur, A.: Improved structural and magnetic properties of cobalt nanoferrites: influence of sintering temperature. Ceram. Int. **41**, 4492–4497 (2015)

16. Slonczewski, J.C.: Origin of magnetic anisotropy in cobalt-substituted magnetite. Phys. Rev. **116**(6), 1341–1348 (1958)

17. Kumar, L., Kumar, P., Kar, M.: Cation distribution by Rietveld technique and magneto-crystalline anisotropy of Zn substituted nanocrystalline cobalt ferrite. J. Alloys Compd. **551**, 72–81 (2013)

18. Kumar, L., Kar, M.: Influence of Al^{3+} ion concentration on the crystal structure and magnetic anisotropy of nanocrystalline spinel cobalt ferrite. J. Magn. Magn. Mater. **323**(16), 2042–20482121 (2011)